A New Manganite with an Original Composite Tunnel Structure: $Ba_6Mn_{24}O_{48}$

Ph. Boullay, M Hervieu, and B. Raveau

Laboratoire CRISMAT, ISMRA et Université de Caen, Bd. Marechal Juin, 14050 Caen Cedex, France

A new manganite $Ba_6Mn_{24}O_{48}$ with an original tunnel structure has been synthesized. Its electron diffraction study shows that this new phase exhibits a composite structure, built up of two tetragonal I sublattices with $a = 18.2$ Å, $c_1 = 2.8$ Å, and $c_2 = 4.6$ Å. The high-resolution electron microscopy investigation shows that the octahedral $[Mn_4O_8]_\infty$ host lattice consists of hollandite- and rutile-type columns sharing the edges of their MnO_6 octahedra so that a new kind of ten-sided tunnel is generated. The powder X-ray diffraction study confirms that the first sublattice (a, c_1) corresponds to the $[Mn_4O_8]_\infty$ framework. The second sublattice (a, c_2) is associated with the barium network. The incommensurate modulated superstructural spots in the "a, c_2" sublattice are correlated to both the occupancy and displacive modulation of the barium ions in the two kinds of tunnels. © 1997 Academic Press

I. INTRODUCTION

The mixed valence of manganese is undoubtedly one of the key factors for the richness of the Ba–Mn–O system, generating a large number of stoichiometric and nonstoichiometric oxides. For example, the structures of the numerous polymorphs of $BaMnO_{3-x}$, first reported by Negas and Roth (1), are directly correlated to the oxygen content. On the other hand, for low barium content, Ba_xMnO_2 with $x \simeq 0.12$ (2) exhibits the hollandite-type structure. These latter oxides correspond to the general formula $A_{2-x}M_{8-\delta}X_{16}$, with $A = $ Ba, Pb, K, Rb, Tl, Na; $M = $ Ti, Mn, Fe, Mg, Mo, Sb, Al, Cr, Ga, … ; and $X = O^{2-}$ or OH^-. These oxides have been intensively examined as solid state electrolytes (3), superionic conductors (4), and, more recently, as possible encapsulators for radioactive waste (5–7).

In fact the solid state chemistry of the tunnel structures in Ba_xMnO_2 are extremely complex. It has been indeed observed that besides the ideal tetragonal hollandite structure, there exist orthorhombic and monoclinic distortions (2, 8–11). But most importantly, modulation and disorder phenomena concerning the particular arrangement of the cations in the large four-sided tunnels are commonly observed (12–17). Moreover, a synthetic hollandite-type has been observed by dehydration of the psilomelane $(Ba, H_2O)Mn_5O_{10}$ (18) at 550°C. Numerous extended defects and phase transitions have been observed for $Ba_xMn_8O_{16}$ (11). This suggests that by varying the experimental conditions, the possibility to stabilize new tunnel structures in this system should be considered.

In this paper, we report the synthesis of a new mixed valent barium manganese oxide $Ba_6Mn_{24}O_{48}$, which exhibits a rare composite tunnel structure, related to rutile and hollandite. The structural investigation of this compound shows that the location of barium atoms inside the tunnels of the MnO_6-based framework is the origin of the incommensurate modulated structure of the compound as well as a disorder phenomenon observed in the form of diffuse streaks in electron diffraction (ED) patterns.

II. EXPERIMENTAL

In a first preparation, $BaCO_3$ and MnO_2 as precursors and Bi_2O_3 as a melting agent were ground in an agate mortar. The mixture was then heated in air according to the following general thermal process: the temperature was increased to 900°C (300°C/h), maintained at this temperature for 20 h, increased to 1200–1270°C (300°C/h), maintained at this temperature for 2 h, and then decreased to room temperature (1°C/h). The Guinier camera photographs showed that the major phase of these preparations did not correspond to hitherto reported materials. Other phases such as hexagonal $BaMnO_3$ isotypes were also present. Two kinds of single crystals were obtained, one kind being hexagonal plates and corresponding to an unusual member (9R) of the $BaMnO_3$ polytypes (19). The second type of single crystals were needle-shaped and corresponded to the new phase. Considering the Weissenberg patterns, the poor quality and small sections of the crystals did not allow us to obtain sufficient diffraction information for a conventional single crystal X-ray study.
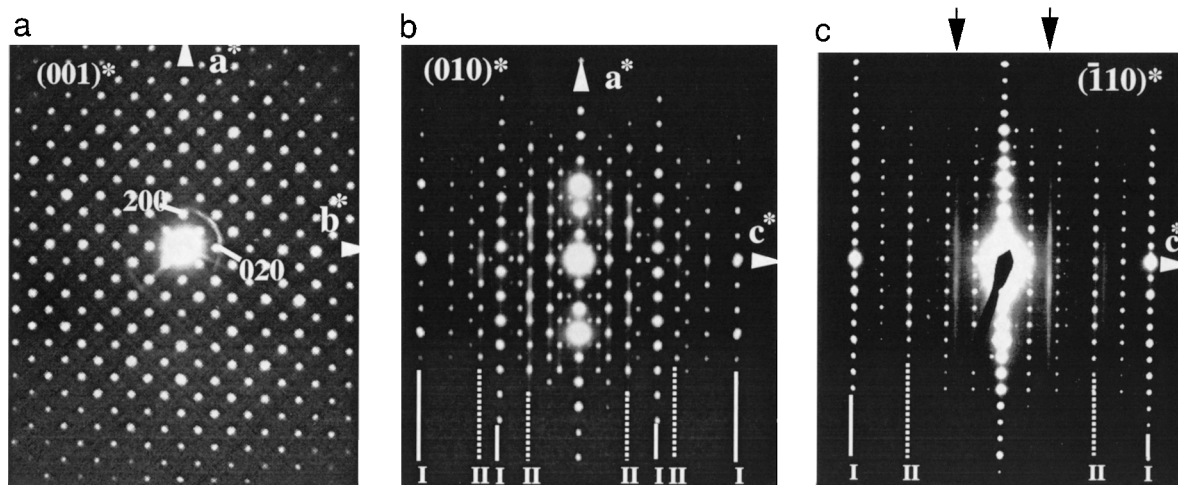
FIG. 1. The [001] ED pattern presented in (a) does not exhibit any satellite reflections, in contrast to the [010] and [110] patterns given in (b) and (c), respectively. For these two latter patterns, two sets of fundamental reflections are considered, denoted I and II. The I centering mode is violated for the second subsystem (diffuse streaks indicated by arrows) in (c).

To obtain polycrystalline samples for Rietveld analysis and to avoid the formation of $BaMnO_3$ polytypes, a second process was used. The starting powders, BaO_2 and Mn_2O_3 (ratio 1/2), were ground, packed in an alumina finger, and sealed in an evacuated silica tube. The samples were heated at $1100°C$ for 20 h and slowly cooled to room temperature. The powder X-ray diffraction patterns were registered on a Philips diffractometer using $CuK\alpha$ radiation and equipped with a graphite back-scattering monochromator. The data were refined with the program Fullprof (20).

The samples for electron microscopy were selected from the needle-shape crystals, crushed in n-butanol, and deposited onto a holey carbon film (copper grid). The electron diffraction (ED) study was carried out with a JEOL 200CX electron microscope fitted with an eucentric goniometer ($\pm 60°$). High-resolution electron microscopy was performed with a TOPCON 002B microscope equipped with a $\pm 10°$ double tilt goniometer and an objective lens with a spherical aberration constant of 0.4 mm. Both microscopes are equipped with KEVEX EDS analyzers. HREM image simulations were carried out with the NCEMSS program (21).

The EDS analyses performed on numerous crystallites confirmed the homogeneity of the sample with a Ba/Mn ratio close to 0.25. Starting from this ratio the oxygen content was estimated by chemical analysis so that the O/Mn ratio was close to 2.

III. ELECTRON DIFFRACTION

The ED patterns give the general characteristic of this new compound. The structure of the reciprocal space appears complex with, besides fundamental reflections, the presence of both diffuse streaks and superstructure reflec-

tions which cannot be simply indexed using three reciprocal vectors.

The fundamental set of reflections corresponds to a tetragonal cell with $a \simeq 18.2$ Å and $c_1 \simeq 2.8$ Å. The conditions limiting the reflections are (hkl): $h + k + l = 2n$ involving an I-type lattice with the possible Laue classes $4/m$ or $4/mmm$. The [001], [010], and [110] patterns showing this set of fundamental reflections are given in Fig. 1. From these ED patterns, it appears that the $(001)^*$ plane is not affected by the modulation wave. For indexing the complete ED patterns, each satellite reflection is attached to a fundamental reflection $(hkl0)$ and indexed $hklm$, where m represents the order of the satellite reflection (Fig.2a). Note that the third order satellites are clearly visible. Every vector $\mathbf{s}^*$ of the reciprocal space can then be expressed using a fourth reciprocal vector leading to $\mathbf{s}^* = h\mathbf{a}^* + k\mathbf{b}^* + l\mathbf{c}^* + m\mathbf{q}^*$. The vector $\mathbf{q}^*$ corresponds to a one-dimensional modulation wave parallel to $\mathbf{c}^*$, with $\mathbf{q}^* = 0.36\mathbf{c}^*$.

The above set of reciprocal vectors allows a complete indexation of the reciprocal space. However, some particular
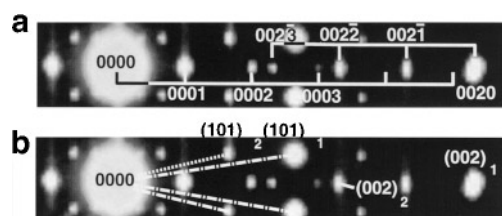

FIG. 2. Indexations of the [100] ED pattern according to: (a) an incommensurate modulated structure; (b) a composite structure, where $[101]^*$ and $[\bar{1}01]^*$ are drawn for both subsystem. The reflections denoted $(101)_1$, $(002)_1$, $(101)_2$, and $(002)_2$ would correspond to the reflections 1010, 0020, 1001, and 0002, respectively, considering $\mathbf{s} = h\mathbf{a}^* + k\mathbf{b} + l\mathbf{c}_1^* + m\mathbf{c}_2^*$.
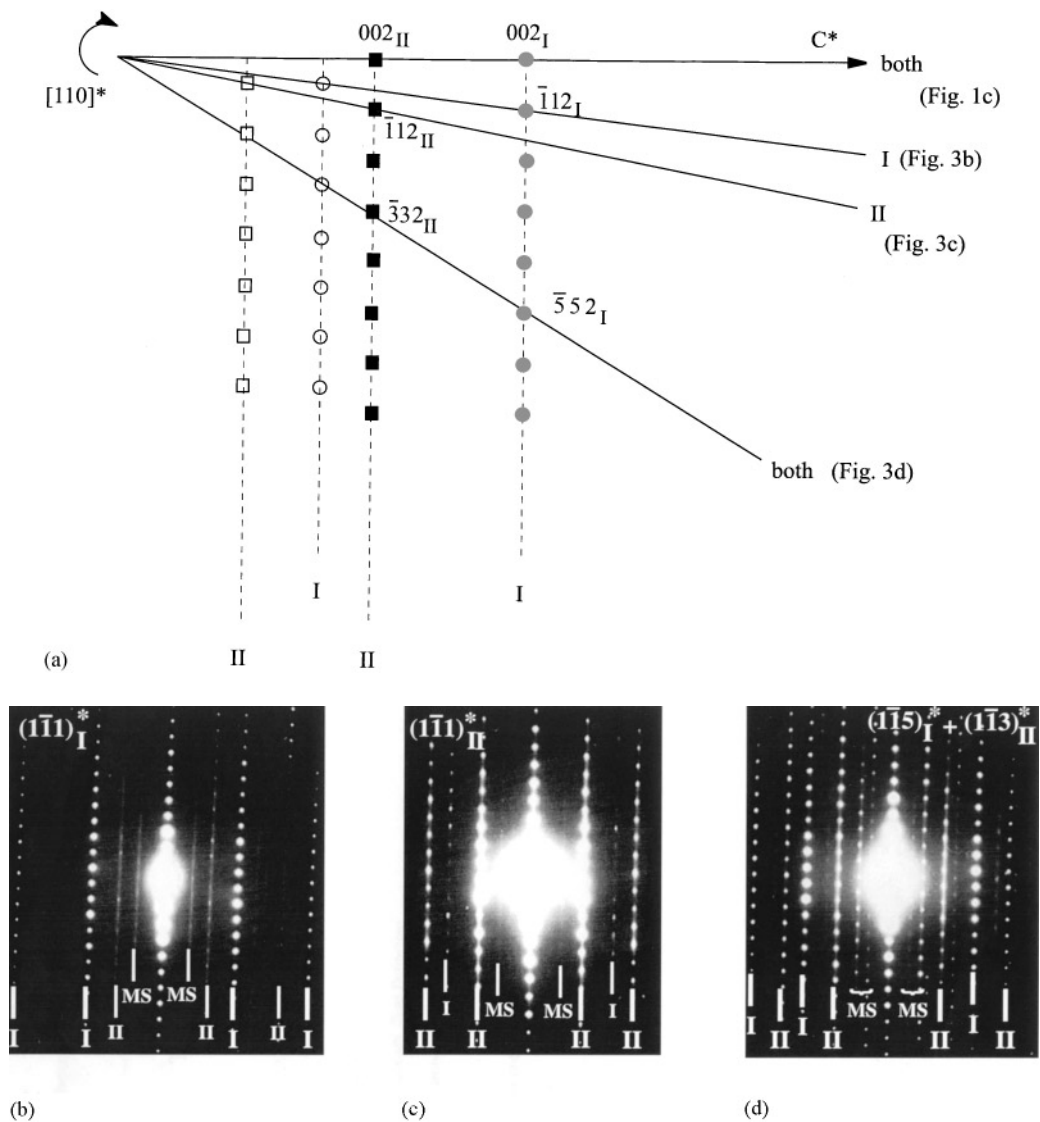
FIG. 3. (a) Schematized projection along $[110]^*$ of the reciprocal space. The ED patterns selected in (b), (c), and (d) show the existence of two distinct sets of fundamentals reflections. These three ED patterns are indexed for each subsystem, denoted I ($a \approx 18.2$ Å and $c_1 \approx 2.8$ Å) and II ($a \approx 18.2$ Å and $c_1 \approx 4.6$ Å). The diffraction spots or lines produced by multiple scattering are denoted by MS. Note that in (b), due to the softening of the conditions of diffraction, residual diffraction from the $(1\bar{1}1)^*_{II}$ plane is observed in the $(1\bar{1}1)^*_I$ plane and reciprocally in (c).

characteristics encountered during the electron diffraction study are not well explained. For instance, in the [110] ED patterns we notice that the intensities of satellites do not decrease as their order increases (Fig. 1c) unlike the $(010)^*$ plane (Figs. 1b and 2). This phenomenon is more striking when investigating the reciprocal space, tilting along $[110]^*$. It clearly appears that in fact two sets of fundamental reflections can be distinguished. To illustrate this point, three patterns are selected in Figs. 3b, 3c, and 3d; the corresponding projection along $[110]^*$ is schematically drawn in Fig. 3a where the two subsystems are denoted I and II. The first set, denoted I, is associated with the above-described cell, i.e., $a \approx 18.2$ Å, $c \approx 2.83$ Å. It presents sharp diffraction spots (Fig. 3b alone; Figs. 1b, 1c, and 3d

together with the second set). The second set, denoted II, corresponds to $a \approx 18.2$ Å, $c \approx 4.6$ Å. It exhibits elongated diffractions spots and diffuse streaks (Fig. 3c alone; Figs. 1b, 1c, and 3d together with the first set). The structure should no longer be considered as a conventional incommensurate modulated structure but as a composite structure where two subsystems coexist, having their own, but mutually incommensurate, translational symmetry. According to this the two subsystems have both tetragonal cells and are defined as in Table 1.

The $(001)^*$ plane exhibits a unique array of sharp spots since the two subsystems have a common mesh in this reciprocal plane. The $(010)^*$ and the $(\bar{1}10)^*$ planes can be indexed using the set $M = \{\mathbf{a}*, \mathbf{b}*, \mathbf{c}_1^*, \mathbf{c}_2^*\}$ of reciprocal

TABLE 1

Subsystem 1	Subsystem 2
$S1 = (\mathbf{a}, \mathbf{b}, \mathbf{c}_1)$	$S2 = (\mathbf{a}, \mathbf{b}, \mathbf{c}_2)$
$a \simeq 18.2$ Å and $c_1 \simeq 2.8$ Å	$a \simeq 18.2$ Å and $c_2 \simeq 4.6$ Å
I-type lattice $(hkl)_1 : h + k + l = 2n$	I-type lattice $(hkl)_2 : h + k + l = 2n$
Laue class: $4/m$ or $4/mmm$	Laue class: $4/m$ or $4/mmm$

vectors. Every vector $\mathbf{s}^*$ of the reciprocal space is expressed as $\mathbf{s}^* = h\mathbf{a}^* + k\mathbf{b}^* + l\mathbf{c}_1^* + m\mathbf{c}_2^*$; the first subsystem gives rise to $hkl0$ reflections and the second to $hk0m$ reflections (Fig. 2b). The diffuse streaks are systematically associated to the second subsystem and indicate that a disorder phenomenon is attached to this subsystem. No diffuse scattering is generated by the first subsystem. The $hklm$ reflections with $h \neq 0$ and $k \neq 0$ correspond to satellite reflections which are common to both subsystems. The intensities of these satellite reflections are mainly produced by double diffraction between the two sublattices. Hence some rows of pure satellite reflections appear streaked because the second subsystem generates diffuse linear scattering (Fig. 1b and 3d). Similar disorder phenomena are observed in other hollandite-type compounds (22) and also in some composite structures, such as $(Sr, Ca)_{14}Cu_{24}O_{41}$ (23), but this will be discussed later. Moreover, diffuse streaks are observed, perpendicularly to $\mathbf{c}_2^*$ (see arrows in Fig. 1c), showing that the I-type symmetry is violated in the second subsystem.

IV. THE [001] HREM IMAGES

The c_1 parameter of the tetragonal subcell, 2.83 Å, is the classical value observed in the rutile-, hollandite-, or psilomelane-type structures and strongly suggests a structure built up from a manganese octahedral framework forming tunnels where the barium atoms would be located. However, the geometrical relationships of the a subcell parameter with the others are not straightforward. To understand the structure, the high-resolution electron microscopy study was carried out in several steps. The structure was first observed along $\mathbf{c}$, i.e., viewing the common plane.

Typical images of the experiment through focus series recorded for the new structure are displayed in Fig. 4. The interpretation of the contrast of the [001] HREM images can be made with the help of calculated images of the rutile and hollandite structures.

In Figs. 4a and 4c, the barium columns are assumed to be imaged as very bright dots whereas in Fig. 4d they would appear as dark spots surrounded by a grey circle. On one hand, the barium atoms form a square array of single dots (13 Å spaced) and on the other hand we note the existence of double dots (4 Å spaced). This suggests that there exist two

types of tunnels in the structure: one which would be filled by a single barium column and a second with two adjacent barium columns. In the structure, along the [110] direction, one single dot alternates with one double dot, the two adjacent dots being aligned along [$\bar{1}$10]. The barium atoms are thus projected onto the (a, b) plane as represented on the schematic drawing in Fig. 5 with respect to cell parameters found by ED.

To find out the structural framework, namely the positions of the manganese atoms, we used the rutile and hollandite simulated images. In the hollandite structure, the barium atoms are aligned in the tunnel (H) so that one observes a square array of bright dots, spaced 6.9 Å along [110] in agreement with the I-type symmetry. The calculated image for a focus value close to -600 Å and a crystal thickness of 17 Å where the barium columns appear as bright dots is given in Fig. 6a. As a starting point, we assumed the single barium columns observed in the new structure were similar to the single barium columns observed in the hollandite. Then, coming back to the enlarged view of Fig. 4c (Fig. 6b), one observes eight small grey dots around every single bright dot; they were assumed to correspond to the manganese positions forming the hollandite tunnels (large squares H in Fig. 5). The four small grey dots could be associated to the contrast observed for manganese atoms forming a rutile tunnel (small squares labeled R in Fig. 5). The structural framework is made up by a regular succession of rutile and hollandite columns along the [100] and [010] directions of the cell as schematized in Fig. 5.

V. X-RAY POWDER DIFFRACTION

Considering the arrangement of the manganese atoms around the barium cations, one can propose that a hollandite column is connected to a rutile column along $\mathbf{a}$, by sharing the edges of their octahedra as schematized in Fig. 5, leading to the ideal framework $Ba_{10}Mn_{24}O_{48}$. Such an arrangement can be repeated for the entire cell provided we keep the $I4/m$ Laue class.

With the actual volumic cell (≈ 940 Å^3 taking $c_1 \approx 2.83$ Å) and the great number of structural parameters, using the Rietveld method to solve such a structure would be a tricky problem. Moreover, due to the poor quality of the data obtained from a standard X-ray diffractometer the refinement of the incommensurate structure cannot be reasonably achieved with accuracy, but it is of high interest to check the proposed model. For the time being, we will not take into consideration the incommensurability and we will perform the refinement using the following process.

At the first stage only the $hk0$ reflections common to both subsystems are used. This allows the determination of the atomic parameters of the projected structure along [001]. From these atomic parameters the z coordinates were
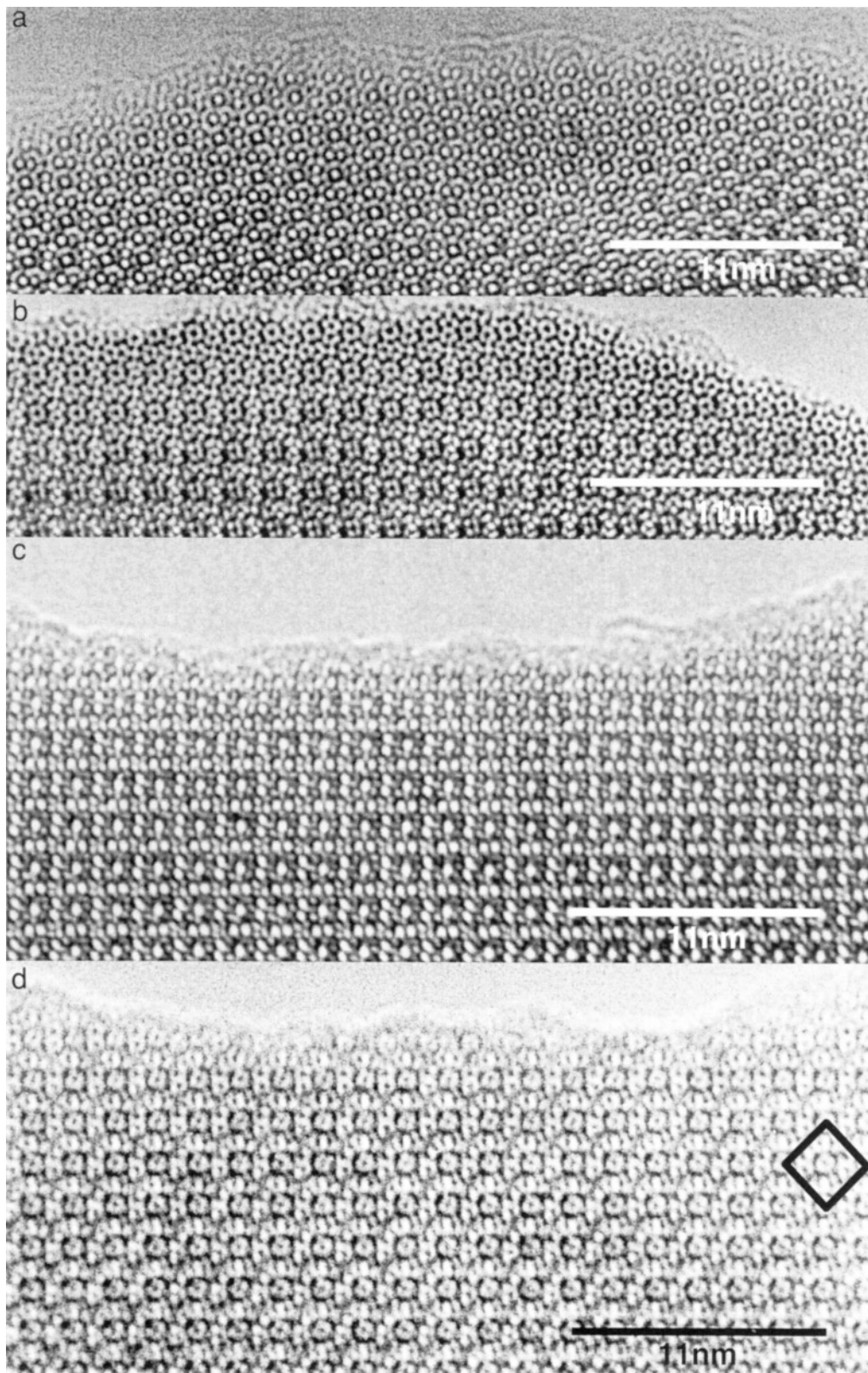
FIG. 4. Typical experimental [001] HREM images selected from the through focus series for the compound $Ba_6Mn_{24}O_{48}$. The focus values range between $+50$ and -1100 Å, from (a) to (d). The unit cell (18.2×18.2 Å) is drawn in (d).
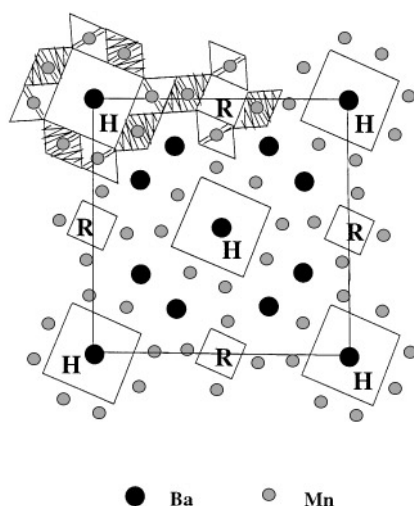
FIG. 5. Schematized projection of the cation positions along **c**. The hollandite H tunnels contain barium ions (large filled circles). The manganese atoms that form the framework are represented by small filled circles.
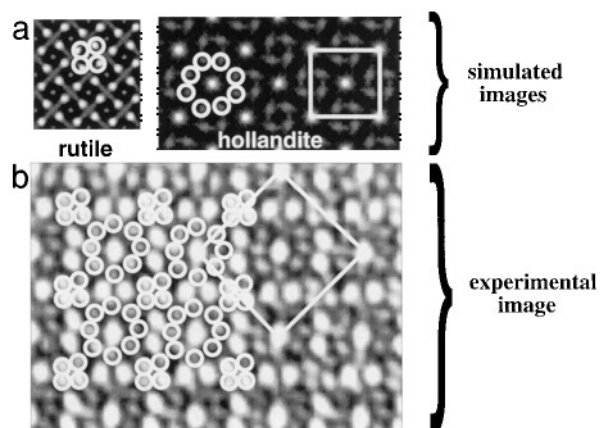

FIG. 6. Comparison of the simulated [001] HREM images of the rutile and hollandite structures with the experimental images observed for the new compound. The manganese positions are represented by white open circles.

assumed to be either $z = 0$ or $z = 0.5$. The manganese and oxygen sites were assumed to be fully occupied. The thermal agitation parameters of oxygen atoms were fixed to $1\ \text{Å}^2$. The global occupancy of the barium sites was refined and found to be slightly higher than 60%. Such a value is in agreement with the Ba/Mn ratio observed by EDS and leads to the cationic content of "Ba_6Mn_{24}" per cell. To account for the incommensurability and fit the whole pattern the choice was made to use anisotropic thermal agitation factors for the barium atoms. As expected, the thermal agitation appears strongly anisotropic along the **c** axis for

both barium sites with mean square displacements of 0.25 and $0.29\ \text{Å}^2$. These values are consistent with an incommensurate modulation along the **c** axis which can produce such displacements. In Fig. 7, the calculated and experimental patterns are plotted together. The atomic parameters are displayed in Table 2 and interatomic distances in Table 3. Soft distance constrains were applied to ensure that the Mn–O distances are close to those observed for similar structures. As expected, the reliability factors are high ($\chi^2 = 5\%$, $R_{\text{Bragg}} = 11.4\%$, and $R_{\text{wp}} = 25.9\%$), as the standard deviations of most of the parameters. Nevertheless, this XRPD study is of high interest since it strongly supports the

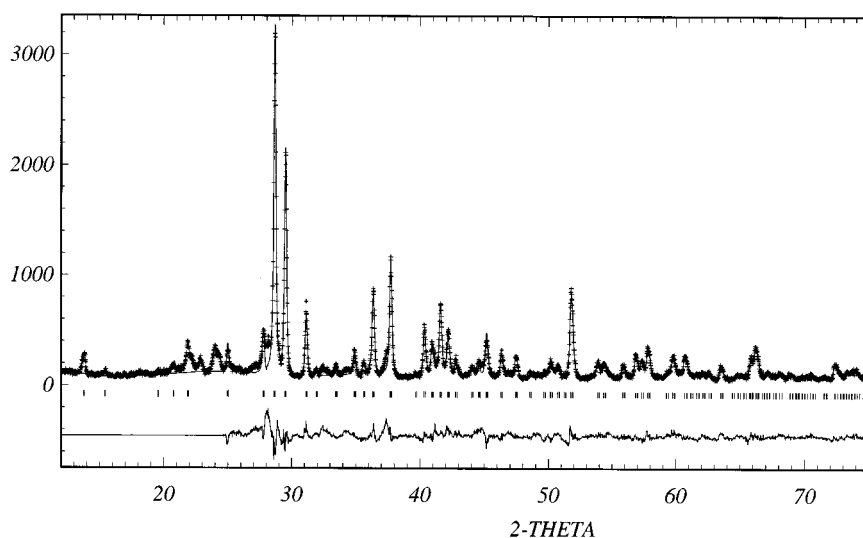**FIG. 7.** X-ray powder diffraction pattern of the $Ba_6Mn_{24}O_{48}$ compound. The experimental, calculated, and difference patterns are represented. From the marks indicating the $Ba_6Mn_{24}O_{48}$ reflections, considering the cell of the first subsystem ($18.2 \times 18.2 \times 2.8\ \text{Å}$), some reflections remain unindexed at low angle.

TABLE 2

Atomic parameters for $Ba_xMn_4O_{8-\delta}$
SG: $I4/m$ (No. 87), $a = 18.173(2)$ Å, $c = 2.836(1)$ Å

Element	x	y	z	B (Å^2)	Site	Occupancy
Ba_1	0	0	0.5	*	$2b$	0.71(3)
Ba_2	0.316(2)	0.170(2)	0.5	*	$8h$	0.61(1)
Mn_1	0.215(1)	−0.005(2)	0	0.9(5)	$8h$	1
Mn_2	0.370(2)	−0.006(2)	0.5	1.3(6)	$8h$	1
Mn_3	0.373(2)	0.347(2)	0	1.3(6)	$8h$	1
O_1	0.313(4)	0.040(5)	0	1.00	$8h$	1
O_2	0.115(5)	0.934(4)	0	1.00	$8h$	1
O_3	0.588(6)	0.062(5)	0	1.00	$8h$	1
O_4	0.193(5)	0.183(5)	0	1.00	$8h$	1
O_5	0.440(4)	0.244(5)	0	1.00	$8h$	1
O_6	0.561(5)	0.319(6)	0	1.00	$8h$	1

*Anisotropic thermal agitation factors

	u_{11}	u_{22}	u_{33}	u_{12}
Ba_1	0.01(1)	0.01(1)	0.25(2)	—
Ba_2	0.03(1)	0.03(1)	0.29(2)	−0.07(1)

FIG. 8. Comparison between experimental and simulated [001] HREM images for a crystal thickness of 17 Å.

structural model based on the combination of hollandite and rutile columns. Moreover it confirms the barium content in the tunnels, in agreement with the EDS analysis. Although there exist large uncertitudes about oxygen positions, this study also shows that the MnO_6 octahedra tend to be distorted, so that a "5 + 1" coordination, intermediate between an octahedral and a square pyramidal coordination, should be considered. Such a geometry is also in agreement with the mixed valence Mn(III)–Mn(IV).

[001] HREM image calculations were therefore carried out for these positional parameters. They show a good agreement between the experimental and calculated contrasts. Some of them are enlarged and directly compared to the experimental ones in Fig. 8 for four focus values and a crystal thickness of 17 Å.

TABLE 3
$Ba_6Mn_{24}O_{48}$ Interatomic Distances (Å)

Ba_1-O_2	2.80(2)	(× 8)	Mn_2-O_3	2.10(4)	
−Ba_1	2.836(−)		−O_5	2.30(3)	
			−O_1	1.94(2)	(×2)
			−O_3	1.91(2)	(×2)
Ba_2-O_1	2.76(3)	(×2)			
−O_3	2.67(3)		Mn_3-O_5	2.23(4)	
−O_4	2.67(3)	(×3)	−O_6	1.94(2)	(×2)
−O_5	2.99(3)	(×2)	−O_2	1.93(2)	(×2)
−Ba_2	2.836(−)	(×2)	−O_4	1.93(2)	(×2)
Mn_1-O_1	1.95(3)				
−O_2	2.14(3)				
−O_5	1.88(2)	(×2)			
−O_6	1.95(2)	(×2)			

VI. DESCRIPTION OF THE $[Mn_4O_8]_\infty$ HOST LATTICE

From the HREM and XRPD results, the $Ba_6Mn_{24}O_{48}$ phase should be formulated. The projection of the $[Mn_{24}O_{48}]_\infty$ framework onto the (001) plane is shown in Fig. 9. One recognizes rutile (R) and hollandite (H) columns running along **c**. These two blocks adopt a face centered arrangement. In fact, the entire $[Mn_{24}O_{48}]_\infty$ framework can be described by the assemblage of these two kinds of columns that share the edges of their octahedra in the (001) plane. It results in three kinds of tunnels: the hollandite tunnels built up of four double octahedral chains that contain single rows of barium ions, the rutile tunnels built up of four octahedral chains that are empty, and a new kind of tunnel bordered by 10 MnO_6 octahedra and containing two barium rows. In this third type of tunnel, one observes two columns of MnO_6 octahedra that exhibit one free oxygen apex per octahedron. These tunnels, due to the existence of free apices and the constriction in their middle, could be compared to the "double barreled" tunnels of $Na_xFe_xTi_{2-x}O_4$ (24), which are occupied by doubled rows of sodium atoms; these double tunnels are therefore denoted (D).

Another way to describe the octahedral framework is to consider rutile-type ribbons of edge shared octahedra running along **c**. These ribbons are condensed by edge sharing, giving an open V-shaped group of three octahedra. This
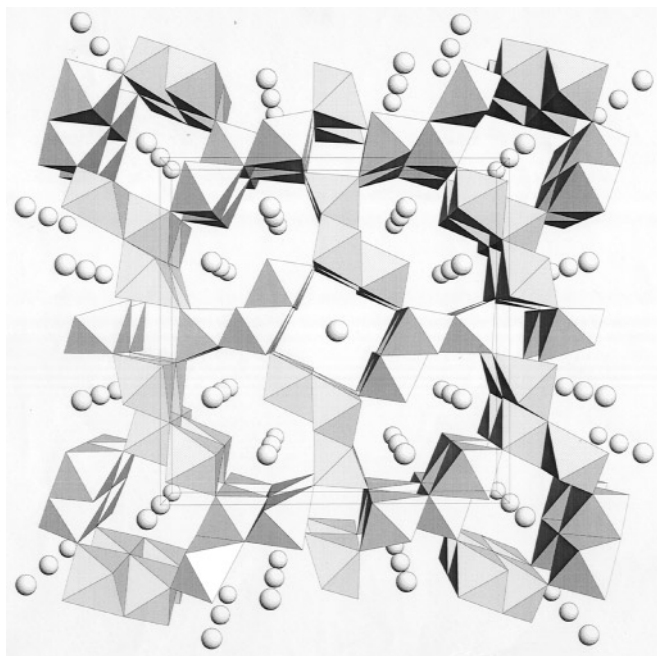
FIG. 9. Perspective view of the $Ba_{10}Mn_{24}O_{48}$ structure where the barium sites would be fully occupied. In the real incommensurate structure, $Ba_6Mn_{24}O_{48}$, the barium atoms are likely to be strongly displaced.

V section runs in an infinite triple ribbon $[Mn_3O_8]_\infty$ along **c**. These ribbons can be compared to the Z-shaped quadruple ribbons, Mn_4O_{10}, observed in $Na_xFe_xTi_{2-x}O_4$ (24). The $[Mn_3O_8]_\infty$ triple ribbons are linked together by sharing four of their five free oxygen apices.

Finally, it is worth pointing out that no defect was detected and that the contrast at the level of the barium columns is regular, whatever the type of tunnel may be, suggesting that the average tunnel occupancy is constant.

VII. DISTRIBUTION OF THE BARIUM ATOMS

In hollandite-type compounds commensurate and incommensurate superstructure reflections and diffuse scattering are commonly observed (12–17, 22). Several models of atoms distributions within the tunnels have been proposed. In this new structure similar phenomena occur. The rising of the second set of fundamental reflections in the ED patterns, and more generally the existence of incommensurate super-structural sharp spots, would be correlated to the ordering of the barium atoms within the tunnels and the interactions between tunnels.

As shown by the interatomic distances calculated from the XRPD model, sites suitable for barium atoms exist inside tunnels (H and D). Sites are potentially present but cannot be fully occupied since the periodicity imposed by the octahedral framework does not correspond to the ideal distance between large cations within a tunnel. In terms

of incommensurate modulated structures this will involve both occupancy and displacive modulations. This is illustrated in hollandite-type compounds with the compound $La_{1.16}Mo_8O_{16}$ (17) but also in other tunnel structures such as $Ba_{0.85}Ca_{2.15}In_6O_{12}$ (26). In the present structure barium atoms seem to adopt their own mean periodicity along the **c** axis. But we cannot state whether this phenomenon occurs in both or in only one kind of tunnel.

The second phenomenon is the disorder attached to the second subsystem. This can be explained by an initial phase disorder (IPD) between the different columns of barium belonging to the second subsystem. It has been proved mathematically (25) that such initial phase disorder in a one-dimensional displacive modulation modifies the reciprocal space and produces diffuse scattering. This can also be applied for columnar composite structures (22). Here the diffuse diffraction lines are always associated to the sharp spots of the second set of fundamental reflections. This corresponds to situations where the initial phase is partially disordered; i.e., from channel to channel some barium atoms will not have the same z position as the main barium network. There exist interactions between the barium atoms in adjacent tunnels, otherwise no sharp spots would be observed, but these interactions are too weak to ensure an ordered initial phase for the second subsystem.

The observation and the interpretation of such complex features are not straightforward, even when the crystals are viewed perpendicularly to **c**.

The [010] zone axis was selected since the hollandite-type single columns are projected onto a single line and the double columns of the D tunnel into two lines (Fig. 10a). The calculated images carried out based on the XRPD model show that for a focus value close to -550 Å, the contrast consists in a double row of staggered bright blobs for the two columns of the D tunnels and in a single row of smaller bright blobs for the Ba atoms in the hollandite tunnels. They are indicated by two black triangles and one white triangle, respectively, in Fig. 10b which is assumed to be recorded for such a focus value.

In the thinnest edge of the crystal, we can expect that the number of projected barium onto a position is small enough to allow a few significant interatomic distances to be visualized. At the level of the double tunnels, a distance of 4.6 Å between two bright dots is often observed along **c** whereas the dots of the adjacent column are in staggered positions. This is in agreement with the periodicity expected for the second subsystem. Such an arrangement indicates that the Ba of the two adjacent columns are spaced 4.6 Å apart, which is also in agreement with the occupancy factor. However, this periodicity is not perfectly established throughout the whole crystal along **c**, but only in domains over a few nanometers long. One also observes small shifts in the barium positions along **c**, from one double tunnel to the adjacent tunnels. This was expected in the case of an IPD
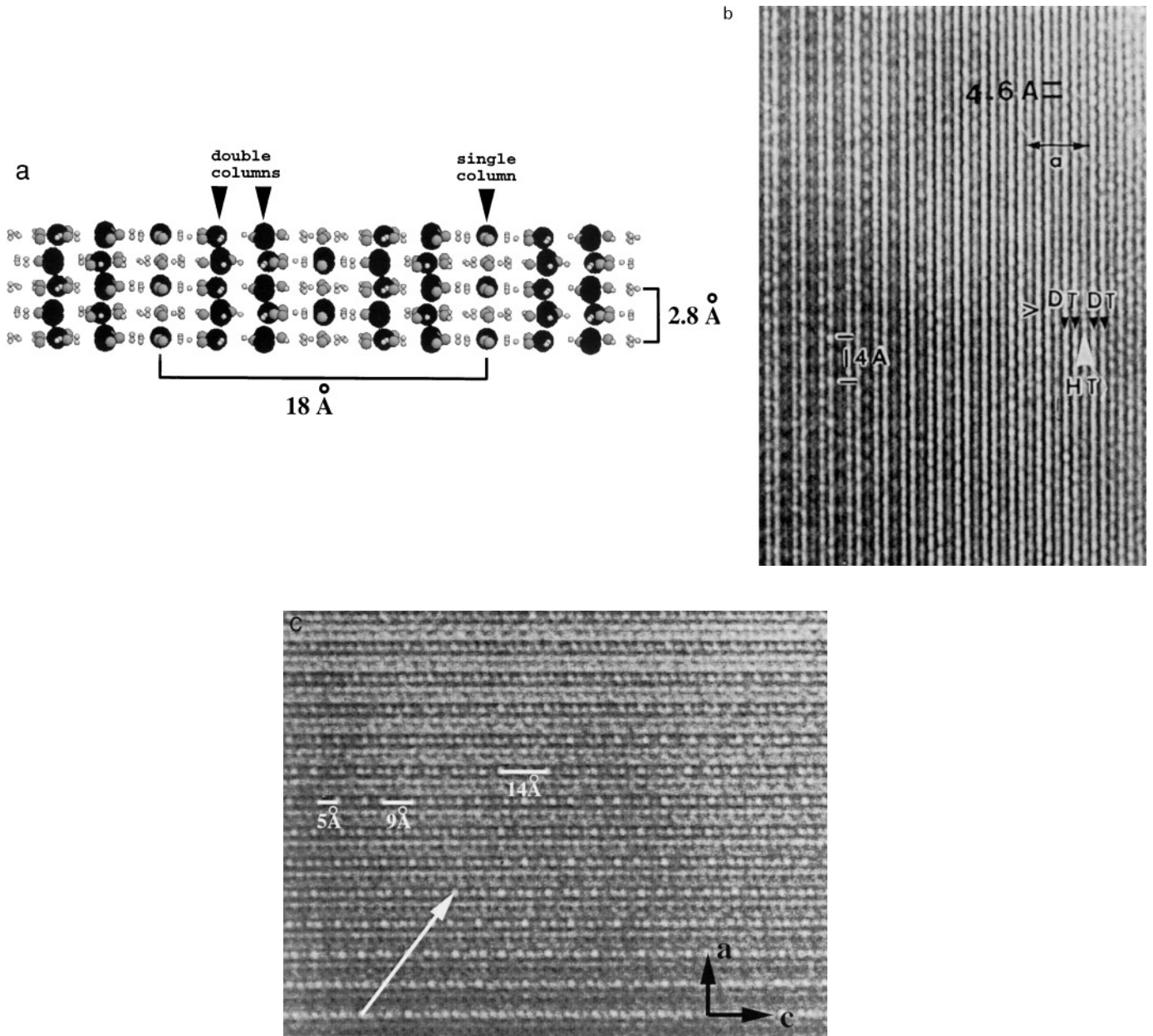
FIG. 10. (a) Projection along [010] of the $Ba_{10}Mn_{24}O_{48}$ structure. Barium, manganese, and oxygens atoms are represented as large black circles, medium grey circles, and small white circles, respectively. (b) [010] HREM image for a focus value close to -550 Å. The double barium columns are denoted DT (black arrows) and the single one HT (white arrow). In the double tunnels, nodes corresponding to the 4.6 Å periodicity are locally observed for the barium atoms. (c) [010] HREM image for a focus value close to -200 Å. In the thicker part of the image (bottom) the pseudo-periodicity of 14 Å (near commensurate supercell corresponding to 2.8×5 Å and 4.6×3 Å) is evidenced when looking at glazing incidence in the direction of the white arrow.

model and explains the diffuse scattering attached to the second subsystem. These features could also explain that only small domains with a 4.6 Å periodicity are observed. In the same way when the shifts are of importance, the **c**/2 translation should not be respected and would originate the loss of the I-type symmetry observed in some ED patterns.

For a focus value close to -200 Å, the zones of light electron density appear as bright blobs. When the thickness increases, the empty space between the two double Ba rows is not imaged as a continuous bright row as observed on the crystal edge. Instead some bright nodes appear distributed with alternating 5.2 and 8.6 Å spacings (Fig. 10c). This can be explained as the result of the interference of the two

periodicities along the **c** axis. Supposing indeed two regular phenomena with periods of 4.6 and 2.83 Å and summing these phenomena, maxima appear with 5.2 and 8.6 Å spacings.

At the level of the hollandite tunnels, the contrast is more confused so that no accurate information was obtained from the HREM images about the barium distribution within these tunnels. When nodes are observed they cannot be easily related to the 4.6 Å periodicity observed for the second subsystem along **c**.

VIII. CONCLUDING REMARKS

The study of the new manganite $Ba_6Mn_{24}O_{48}$ shows the complex crystal chemistry of this material, in spite of its close relationships with the hollandite and rutile structures. The complete structure indeed appears as the coexistence of two substructures, one corresponding to the "$Mn_{24}O_{48}$" framework and a second to the "Ba" chains located inside the double tunnels D. No evidence for a specific lattice can be found for the barium atoms located in the hollandite tunnels which are likely to adapt the periodicity of the host framework via an incommensurate modulated structure. The two columnar substructures are both parallel to a common axis (**c**) but with an unequal periodicity along this axis. In the plane perpendicular to the columns axis, the two substructures fit together in a common array and thus have a common $hk0$ plane in reciprocal space. In the present material, the a and b axis in the real space are common.

Although columnar composite crystals have been currently observed in organic compounds (27, 28) such phenomena are rare for oxides. This is in fact the first oxide with a composite tunnel structure. In this respect, it is to be compared with the oxide $Tl_x[SrO]_n[CoO_2]$ which is the only oxide with a layer composite structure (29), in contrast to heavy metal sulfides that form a large family of so-called "misfits" (30).

The complete determination of this complex incommensurate structure, and especially the knowledge about the related disorder, will require the collection of high quality data. The possibility of using synchrotron radiation facilities on small single crystals or on a powder sample in a high-resolution diffractometer is being considered.

REFERENCES

1. T. Negas and R. S. Roth, *J. Solid State Chem.* **3,** 323 (1971).
2. A. Byström and A. M. Byström, *Acta Crystallogr.* **3,** 146 (1950).
3. P. Hagenmuller and W. Van Gool, "Solid Electrolytes," p. 381. Academic Press, New York London.
4. H. U. Beyeler, *Phys. Rev. Lett.* **37,** 1557 (1976).
5. R. W. Cherry, *Acta Crystallogr., Sect. B* **42,** 229 (1986).
6. L. A. Bursill and D. J. Smith, *J. Solid State Chem.* **69,** 343 (1986).
7. A. E. Ringwood, "Safe Disposal of High Level Nuclear Reactor Wastes: A New Strategy," Australia National Univ. Press, Canberra, 1978.
8. R. W. Cheary, *Acta Crystallogr., Sect. B* **46,** 599 (1990).
9. J. P. Parent, R. Olazcuaga, M. Devalette, C. Fouassier, and P. Hagenmuller, *J. Solid State Chem.* **3,** 1 (1971).
10. C. Fouassier, C. Delmas, and P. Hagenmuller, *Mater. Res. Bull.* **10,** 443 (1975).
11. L. C. Nistor, G. Van Tendeloo, and S. Amelinckx, *J. Solid State Chem.* **109,** 152 (1994).
12. L. A. Bursill and G. Grzinic, *Acta Crystallogr., B* **36,** 2902 (1980).
13. S. B. Xiang, H. F. Fannn, X. J. Li, and Q. Pan, *Acta Crystallogr. A* **46,** 929 (1990).
14. C. C. Torardi and J. C. Calabrese, *Inorg. Chem.* **23,** 3281 (1984).
15. C. C. Torardi and R. E. McCarley, *J. Solid State Chem.* **37,** 393 (1981).
16. A. Pring, D. J. Smith, and D. A. Jefferson, *J. Solid State Chem.* **46,** 373 (1983).
17. H. Leligny, Ph. Labbe, M. Ledesert, B. Raveau, C. Valdez, and W. H. McCarroll, *Acta Crystallogr. B* **48,** 134 (1992).
18. A. D. Wadsley, *Acta Crystallogr.* **6,** 433 (1963).
19. Ph. Boullay, M. Hervieu, Ph. Labbe, and B. Raveau, *Mater. Res. Bull.* **32,** 35–42 (1997).
20. J. Rodriguez-Carjaval, "Proc. Satellite Meeting on Powder Diffraction of the XV Congress of Int. Union of Crystallography, Toulouse, France, July 1990".
21. R. Kilaas, "NCEMSS v1.6 October 1996," National Center for Electron Microscopy, Materials Sciences Division, Lawrence Berkeley Laboratory, University of California, Berkeley, CA 94720.
22. X. J. Wu, S. Fujiki, M. Ishigame, and S. Horiuchi, *Acta Crystallogr. A* **47,** 405 (1991).
23. O. Milat, G Van Tendeloo, S. Amelinckx, M. Mehbod, and R. Deltour, *Acta Crystallogr. A* **48,** 618 (1992).
24. W. G. Mumme and A. F. Reid, *Acta Crystallogr. B* **24,** 625 (1968).
25. X. J. Wu and S. Horiuchi, *Acta Crystallogr.* **47,** 11 (1991).
26. G. Baldinozzi, F. Goutenoire, M. Hervieu, E. Suard, and D. Grebille, *Acta Crystallogr. B* **52,** 780 (1996).
27. V. Petricek, K. Maly, Ph. Coppens, X. Bu, I. Cisarova, and A. Frost-Jensen, *Acta Crystallogr. A* **47,** 210 (1991).
28. Ph. Coppens, *Acta Crystallogr. B* **51,** 402 (1995).
29. Ph. Boullay, B. Domenges, M. Hervieu, D. Groult, and B. Raveau, *Chem. Mater.* **8,** 1482 (1996).
30. G. A. Wiegers and A. Meerschaut, *J. Alloys Compounds* **178,** 351 (1992).